communications physics

Article

https://doi.org/10.1038/s42005-024-01608-7

Spin-wave-driven tornado-like dynamics of three-dimensional topological magnetic textures

Check for updates

Lei Qiu [1,2], **Laichuan Shen** [1,2] & **Ka Shen** [1,2] ✉

The abundant topological magnetic textures in three-dimensional systems provide opportunities to investigate the fundamental spin dynamics and realize spintronic applications. The dynamics of such magnetic textures have however rarely been studied, especially for those driven by spin waves, which allow applications with ultralow energy consumption and ease of implementation even in insulating systems. Here, we report our micromagnetic simulations on the spin-wave-driven dynamics of a skyrmion tube (SkT) and chiral bobber (ChB) in a thick magnetic film. We predict tornado-like dynamics in both SkT and ChB, where the topological centers present a lateral rotation with the rotation centers forming a distorted profile in the thickness direction. While the velocity of SkT scales with the driving power, the ChB motion presents a threshold in the driving field, which is found to depend linearly on its penetration length. This distinct behavior could be useful to differentiate ChB from SkT and estimate its penetration length experimentally.

Topological magnetic textures such as skyrmions[1–3], vortices[4–7] and (bi) merons[8–10], are exotic and versatile topological objects in magnetic material that may provide applications in spintronic devices. The manifestation of these topological textures strongly relies on the material parameters and their environment. For example, an isolated skyrmion can be either of circular shape or of stripe configuration, while the skyrmions in a condensed phase usually form a lattice with circular shapes[11–13]. Studies on skyrmions in two dimensions (2D) have been recently extended to their variants, such as skyrmion bags[14–16] and high-order skyrmions[17], as well as their intriguing dynamics driven by spin-transfer torques[18–20] or spin waves[21–23]. A further extension from 2D to three dimensions (3D) brings in additional family members of the topological magnetic textures, including hopfions[24–28], torons[29,30], chiral bobbers (ChBs)[31–34], etc[35–40], which has recently attracted tremendous attention because of their fantastic dynamic properties[41–46]. Recently, it was demonstrated both theoretically[47] and experimentally[31,32,48] that, in a thick magnetic film, skyrmion tubes (SkTs), skyrmion-type 2D spin texture penetrating through the thickness, and ChBs, broken SkTs terminating at Bloch points (BPs)[32] within the film, can be stabilized simultaneously by a bulk Dzyaloshinskii-Moriya interaction (DMI) with rather good robustness against disturbances thanks to their topological characteristics. The differentiation between them is however challenging as most of the magnetic imaging approaches reflect only their very similar skyrmion-type 2D magnetic texture near the sample surface. As the X-ray ptychography is applicable to reveal their different 3D textures[32,49], the appearance of the BP may provide alternatively easier solutions to distinguish ChBs from SkTs in spintronic devices, according to the distinctive BP-induced phenomena[43,50–54].

To date, electrical manipulation of 3D magnetic structures has been realized via the spin-transfer[34,55–57] or spin-orbit torques[46,58] generated by a spin-polarized current. The typical magnitudes of the current density in those studies however are too large to satisfy the requirement of low power consumption applications. More seriously, the enormous current-induced heating is detrimental to the stability of ChB/SkT. In contrast, the magnetic dynamics driven by spin waves can efficiently reduce the energy consumption and heating effects[59–62], which is however still largely unexplored in 3D systems, especially for the ChBs and SkTs and their back-actions to spin waves. This motivates our present work to investigate the interplay between ChBs/SkTs and spin waves.

Based on micromagnetic simulations, we unveil distinct behaviors between the ChB and SkT dynamics driven by spin waves. Specifically, we find that the velocity of the SkT is proportional to the power of the driving field, while the ChB motion presents a threshold in the driving power of spin waves. In addition, we find tornado-like dynamics of SkTs and ChBs, namely, a dynamic modulation of the magnetic textures during their lateral motion. In the meantime, the spin waves diffracted from the BPs of ChBs are found to deviate from the Rutherford-type scattering previously predicted

---

[1]The Center for Advanced Quantum Studies and Department of Physics, Beijing Normal University, Beijing 100875, China. [2]Key Laboratory of Multiscale Spin Physics, Ministry of Education, Beijing Normal University, Beijing 100875, China. ✉e-mail: kashen@bnu.edu.cn

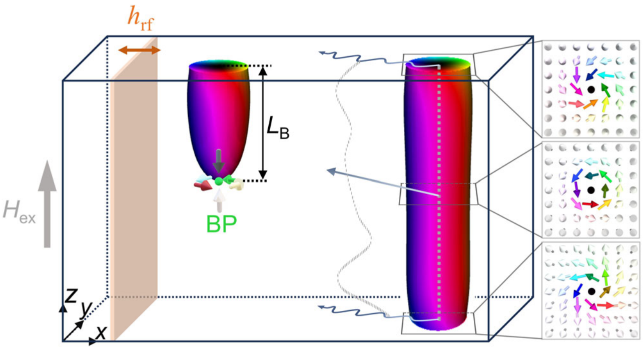

Fig. 1 | Schematic diagram for the simulation of the chiral bobber (ChB) and skyrmion tube (SkT) dynamics driven by the spin waves. Sketch of the simulated geometry with the spin-wave source represented by the khaki region. The left and right solitons correspond to the isosurfaces of $m_z = 0$ for ChB with a penetration length (L_{B}) and SkT, respectively, with the colors indicating the orientation of the in-plane magnetization. The arrows around the end of ChB show the spin configuration of the magnetic Bloch point (BP). The two gray dashed curves describe the spatial profile of the skyrmion centers in SkT along the thickness direction at the static and dynamic states. The thin dark blue arrows indicate the trajectories of the skyrmion centers in the top, middle, and bottom layers. The rightmost panel shows the magnetic structures of the top, middle, and bottom layers in SkT.

from an analytic derivation[50]. These results provide insights for understanding and applying the dynamics of 3D topological magnetic structures.

Results and discussion

Theoretical model

The geometry of our system is schematically shown in Fig. 1. With a perpendicular magnetic anisotropy and an external magnetic field $\mathbf{H}_{\mathrm{ex}}$ applied normal to the film plane, the total micromagnetic energy density thus reads,

$$\begin{aligned}\mathscr{H} =& A(\nabla \mathbf{m})^2 - K_{\mathrm{u}}\left(m_z\right)^2 - \mu_0 H_{\mathrm{ex}} M_{\mathrm{s}} m_z + D\mathbf{m}\cdot(\nabla\times\mathbf{m})\\ &-\frac{1}{2}\mu_0 M_{\mathrm{s}}\mathbf{H}_{\mathrm{dm}}\cdot\mathbf{m},\end{aligned} \tag{1}$$

where A is the stiffness constant, K_{u} is the anisotropy constant, M_{s} is the saturation magnetization and D is the bulk DMI coefficient. $\mathbf{H}_{\mathrm{dm}}$ in the last term corresponds to the demagnetization field. The magnetic parameters and other modeling details are provided in the Methods. Starting from a bobberlike initial state with a proper magnetic field, the energy relaxation due to the Gilbert term leaves a stable ChB structure shown in Fig. 1. Specifically, we set an initial state as all magnetizations within a bobber-shaped region of a given length and a finite radius, pointing opposite to those of the background. After the relaxation process, the initial state finally goes to a stable SkT, ChB, or uniform ferromagnetic phase. For a ChB final state, its penetration length depends on the strength of the external magnetic field and the length of the initial bobber-shaped region. Unless otherwise specified, the magnetic field in the following is set to be $\mu_0 H_{\mathrm{ex}} = 0.18$ T, which stabilizes ChB with a penetration length $L_{\mathrm{B}} = 23$ nm. Alternatively from an initial SkT configuration, the same magnetic field is found to be able to stabilize a SkT as well, where, as shown in Fig. 1, the lateral spin texture presents a dependence on depth due to the demagnetization field.

The spin waves are then introduced to trigger the dynamics of magnetic textures. As the detail of the spin-wave generation may modify the spatial profile of spin waves and hence the response of the magnetic textures, it cannot affect qualitatively the physics. Therefore, in practice, we consider that the spin waves are generated by an AC magnetic field, $\mathbf{h}(t) = h_{\mathrm{rf}}\sin(2\pi f t)\hat{x}$ with a frequency $f = 120$ GHz, in a thin plane of two-unit-cell width illustrated as the khaki region in Fig. 1. In a realistic case with a wider excitation region, a comparable spin-wave intensity can be achieved by a weaker AC magnetic field. The excited spin waves then propagate in the x direction. In order to avoid the reflection at the lateral boundaries, absorbing boundary conditions with gradually enhanced damping is used, while the free boundary condition is applied for the upper and lower surfaces.

To describe the dynamics of ChBs and SkTs, we calculate the temporal evolution of the in-plane topological centers at different values of z from

$$\mathbf{R}(z,t) = \frac{\int \mathbf{r}\rho(\mathbf{r},z,t)dxdy}{\int \rho(\mathbf{r},z,t)dxdy}, \tag{2}$$

in which the topological density is expressed as $\rho = \frac{1}{4\pi}\mathbf{m}\cdot(\partial_x\mathbf{m}\times\partial_y\mathbf{m})$[63]. While the topological centers at the equilibrium configuration form nearly a straight string across the thickness, as shown by the gray dashed curves in Fig. 1 and discussed explicitly below, the presence of spin waves introduces an interesting distortion of linked topological centers and tornado-like dynamics.

Spin-wave-driven dynamics of SkTs and ChBs

The trajectories of the topological centers under the driving field $h_{\mathrm{rf}} = 0.1$ T are plotted in Supplementary Fig. 1 with different values of z. As seen, the topological centers of ChB show only a tiny rotation, while those of the SkT move collectively towards the wave source with a finite Hall angle $\Theta_{\mathrm{H}} \simeq 13.5^{\circ}$. A more explicit analysis of the ChB dynamics (at $z \simeq -L_{\mathrm{B}} = -23$ nm) reveals that the BP actually keeps standing still. The relative motions of the skyrmion centers in ChB with respect to the BP are plotted in Fig. 2a, which clearly shows a larger rotation radius for the skyrmion centers approaching the surface. For the SkT, the trajectories of topological centers at $z = 0$ and -40 nm present clearly wavy vibrations while that at $z = -20$ nm is nearly a simple straight line (see Supplementary Fig. 1). The internal motion of the topological centers within the SkT is thus described by the relative trajectories with respect to the instantaneous location of the topological center at $z = -20$ nm. As depicted in Fig. 2b, the topological center in each layer of SkT, similar to the ChB case, shows nearly circular rotations with the corresponding radius reaching maximal values around the surfaces of the film. As shown in Fig. 2c, the relative rotations of the 2D topological centers in the upper and lower half film are of the same direction but with approximately a π-phase difference, very similar to the spin dynamics of the low-frequency mode in an easy-axis antiferromagnet. Another intriguing feature is that the connection of the rotation centers of SkT surprisingly presents a complicated profile in the y−z plane, i.e., the cross-section perpendicular to the spin-wave propagation direction. Such a distortion is found to be almost a quasi-static configuration during the dynamics and its magnitude becomes larger under a stronger excitation field, which suggests that this distortion should be closely related to the propagation of spin waves. In contrast, the rotation centers of ChB only show a small tilting in the thickness direction. Simulations with different spatial discretization schemes result in very similar features (see Supplementary Fig. 2), which excludes the artificial origin of such tornado-like dynamics. The typical dynamic of the skyrmion at the upper surface of a SkT is shown in Supplementary Movie 1 with $h_{\mathrm{rf}} = 0.4$T.

Origin of the deformation of SkT and ChB

In order to understand the above dynamic features, we derive the bulk dispersion relation of the spin waves as

$$2\pi f = \gamma\left(\mu_0 H_{\mathrm{ex}} + \frac{2K_{\mathrm{u}}}{M_{\mathrm{s}}}\right) + \gamma\frac{2A}{M_{\mathrm{s}}}k^2 + \gamma\frac{2D}{M_{\mathrm{s}}}k_z. \tag{3}$$

As the derivation details are provided in Supplementary Note 1, the spectrum with $k_y = 0$ in our excitation configuration is plotted in Fig. 3a. The presence of the bulk DMI shifts the center of the circular iso-energy surfaces away from $\mathbf{k} = 0$ by $k_{OO'}\hat{z}$ (see Supplementary Fig. 3a). As a consequence, the group velocity of the generated spin-wave with $k_z = 0$ has both x and z components, meaning that the spin waves also travel across the thickness during their propagation in the x direction and undergo reflection at the surfaces. The x and z components of the group velocity of the reflected beam are the same as and opposite to those of the initial spin-wave, respectively,

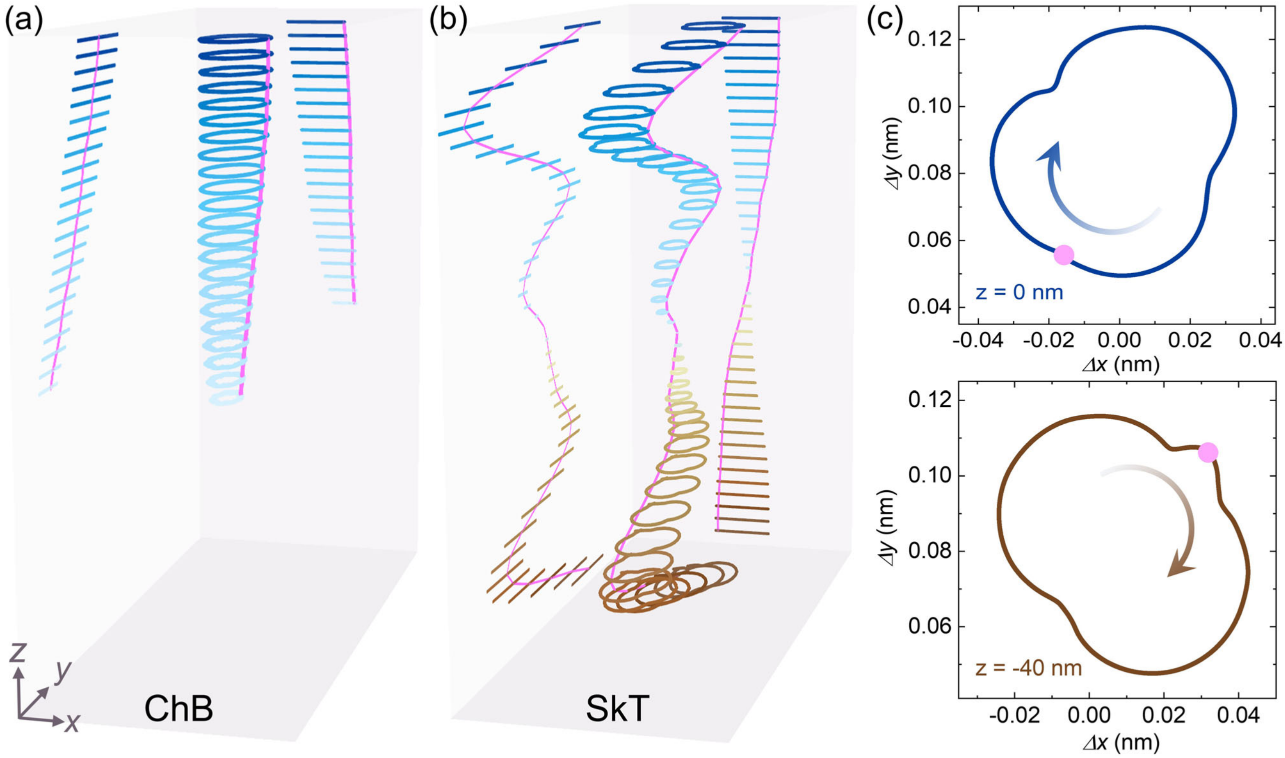

Fig. 2 | Spin-wave-driven tornado-like dynamics of chiral bobber (ChB) and skyrmion tube (SkT). The trajectories of the topological centers and their projections in the $x-z$ and $y-z$ planes for **a** ChB and **b** SkT (with respect to the one at $z = -20$ nm) under the excitation of $h_{\mathrm{rf}} = 0.1$ T. The pink curves stand for the spatial profile of the instantaneous topological centers. **c** The trajectories of the top and bottom topological centers in one period with the arrows and the pink dots indicating the direction of their movements and their positions at a certain moment, respectively.

Fig. 3 | Deformation of chiral bobber/skyrmion tube caused by the nonuniform distribution of spin-wave intensity in the thickness direction. **a** Dispersion relations of the spin waves in the $k_y = 0$ plane. The closed curves in the $k_x - k_z$ plane correspond to the projections of the isofrequency contours at $f = 5$, 15, 30, 60, and 120 GHz. **b** An instantaneous magnetization plot of the spin waves in the $x-z$ plane at $h_{\mathrm{rf}} = 0.1$ T. The color bar represents the x component of the magnetization. **c** The schematic of force analysis for the skyrmions in neighboring layers, S_1 and S_2, with strong and negligible driving force $\mathbf{F}_{\mathrm{drive}}$, respectively. $\mathbf{F}_{\mathrm{M}}$ represents the Magnus force perpendicular to the velocity $\mathbf{v}$ and the purple spring stands for the attractive interaction between the skyrmions. **d** The spatial profile of the skyrmion positions in the $y-z$ plane under the driving field $h_{\mathrm{rf}} = 0.1$ T. The orange areas indicate the regions of high-intensity spin waves.

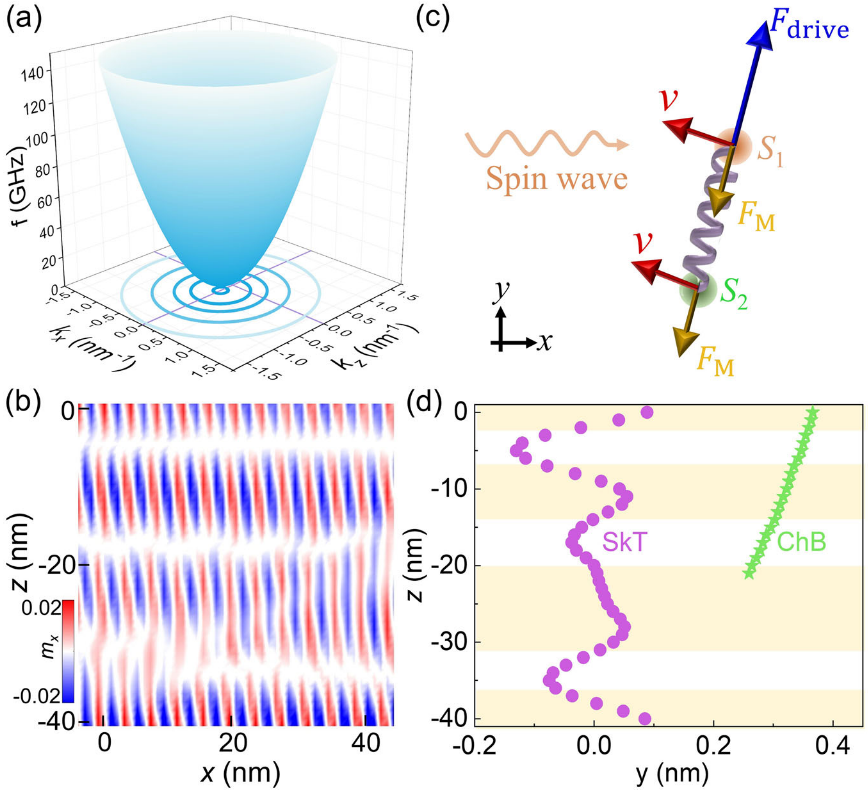

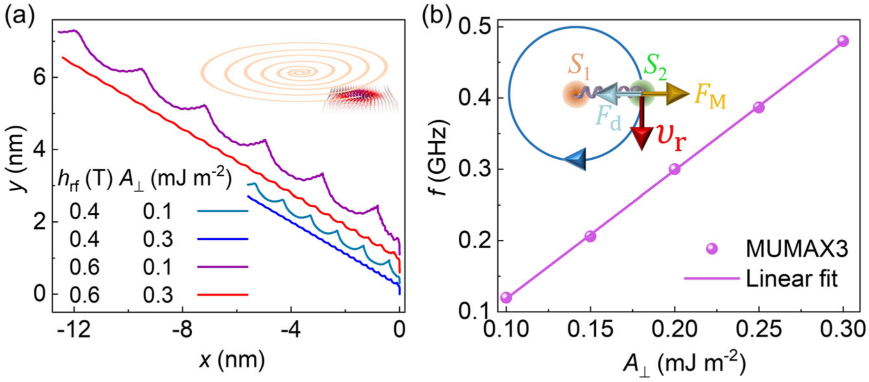

Fig. 4 | Lateral rotation of the topological centers controlled by out-of-plane exchange strength. **a** Trajectories of topological centers at $z = -40$ nm for the first 50 ns, with different values of driving field (h_{rf}) and out-of-plane exchange strength ($A_{\perp}$). A relatively large damping constant $\alpha = 0.01$ is used to magnify the decay rate of the rotation radius. The inset in panel **a** illustrates the long-period evolution of the dissipative rotation of a topological center. **b** Rotation frequency of the topological centers as a function of $A_{\perp}$. The inset in panel **b** is the force analysis of the skyrmion S_2 with a relative velocity $\boldsymbol{v}_{\mathrm{r}}$ with respect to the skyrmion S_1 in its neighboring layer. F_{d} stands for the attractive force from interlayer coupling.

corresponding to the transition of the wave vector from $\mathbf{k}_0$ to $\mathbf{k}_{\mathrm{r}}$ (see Supplementary Fig. 3a). The coherently reflected beam will then cause interference and lead to a considerable modulation of the spin-wave intensity in the thickness direction, giving by $\sim \exp(\mathrm{i}zk_0^z) + \exp(\mathrm{i}zk_r^z)$, where k_0^z and k_r^z correspond to the z components of $\mathbf{k}_0$ and $\mathbf{k}_{\mathrm{r}}$, respectively. By substituting $k_0^z = 0$ and $k_r^z = 2k_{OO'}$, the modulation of spin-wave intensity can be expressed as $1 + \cos(2zk_{OO'})$, which leads to a period of about $\pi/k_{OO'} \sim 12.6$ nm with $k_{OO'} = 0.25$ nm^{-1}, consistent with the numerical results in Fig. 3b and Supplementary Fig. 3b for the distribution of m_x and m_y in the $x-z$ cross-section, respectively. It is found that such a modulation coincides nicely with the spatial distortion of the ChB and SkT shown in Fig. 3d. However, the puzzle remains because the spin waves are pulling the ChB and SkT mainly in the x direction, but the distortion of the topological centers along the thickness counter-intuitively occurs in the y direction.

The solution to this puzzle lies in the requirement of the force balance for the quasi-stationary state of ChB and the uniform lateral motion of SkT. To deduce the driving force from the spin-wave, we consider a skyrmion located in the region with a rather weak spin-wave intensity, i.e., one of the white regions in Fig. 3d, where the driving force acting on the skyrmion is negligibly small. As analyzed in Supplementary Note 2 and sketched in Fig. 3c, the dissipation force is also very weak due to the small damping constant and the Magnus force $\mathbf{F}_{\mathrm{M}}$ of the moving SkT, perpendicular to its velocity, then should be balanced by the dragging force from the 2D skyrmions in the neighboring sublayers. The latter is apparently in the same direction as the relative shift between adjacent 2D skyrmions. Because of the small Hall angle, the Magnus force approximately points to $-y$ direction with $|F_{\mathrm{M}}^y|/|F_{\mathrm{M}}^x| \approx 4.2$, making the weakly driven skyrmions fall behind those experiencing strong driving force along the y-axis (see the pink dots in the white windows in Fig. 3d). For the ChB, the Magnus force, which is proportional to the velocity, is significantly suppressed because of the absence of the net uniform motion and the driving force is mainly compensated by the pinning force of the BP. As a result, the topological centers of the 2D skyrmions form a simple profile in the $y-z$ plane as shown by the green stars in Fig. 3d. Note that in the cases of SkT and ChB, varying the frequencies will not affect our qualitative conclusions. The result of SkT excited by the AC magnetic field at 60 GHz is shown in Supplementary Fig. 4.

Origin of the lateral rotation of topological centers

To further explore the origin of the lateral rotation shown in Fig. 2, an important task is to justify whether it is a persistent rotation or a dissipative one. Therefore, we perform the same simulation as that for Fig. 2 but with a larger damping constant $\alpha = 0.01$. The trajectories of the topological center at $z = -40$ nm are plotted in Fig. 4a for different values of driving field and out-of-plane exchange strength. It can be seen that the wavy amplitude decreases for all cases, indicating clearly the dissipative nature of the lateral rotation. The long-time relative motions of the topological center can therefore be schematically described by the inset in Fig. 4a, where the radius of the rotation orbit gradually shrinks to a single point at the rotation center. This behavior looks similar to the skyrmion motion in an attractive central force field[64]. It is also noteworthy that, the number of the wavy periods in the trajectories is almost independent of the strength of the driving field but strongly relies on the strength of out-of-plane exchange constant $A_{\perp}$, which suggests that the interlayer exchange coupling may provide an attractive force in the present case[65–67]. Note that the value of $A_{\perp}$ can be different from that of A in layered materials or artificial magnetic multilayers[68,69]. For the latter case, $A_{\perp}$ is determined by an adjustable Ruderman-Kittel-Kasuya-Yosida interaction[70]. For a qualitative analysis, we illustrate in the inset of Fig. 4b the forces acting on a skyrmion S_2 which experiences a relative rotation around the other skyrmion S_1 in a neighboring layer. Focusing on the relative motion between S_1 and S_2, we here discard the driving force from spin waves and consider only the radial components of the interlayer pulling force F_{d} and the Magnus force $F_{\mathrm{M}} = Gv_{\mathrm{r}}$, where G and v_{r} represent the gyrovector and the relative motion velocity of the adjacent layer skyrmion, respectively. For the sake of simplification, the dissipation of the S_2 motion is assumed to be sufficiently weak so that the rotation orbit can be regarded approximately as a well-defined circle with the force balance $F_{\mathrm{d}} = F_{\mathrm{M}}$. Assuming further $F_{\mathrm{d}} \approx \eta A_{\perp}\Delta$ with η and Δ being a coupling constant and the distance between S_1 and S_2, respectively[65], we derive the frequency of the rotational motion $f \propto A_{\perp}$, which is confirmed nicely by our micromagnetic simulations (see Fig. 4b). A detailed analysis with the numerical evaluation of η can be found in Supplementary Note 3 and Supplementary Fig. 5.

Velocities of SkT/ChB motion vs. driving field

We now explore the relationship between the velocities of the SkT/ChB and the strength of the driving source. As shown in Fig. 5a, the velocity of the SkT is proportional to the driving power ($\propto h_{\mathrm{rf}}^2$). For the ChB, as discussed above, the spin waves generated by a weak driving field are not sufficient to move the ChB, leading to a vanishing velocity. However, when the driving force is enhanced by increasing the driving field beyond a threshold, the pinning force will be fully compensated, resulting in a collective motion of the ChB. Note that the ChB with a certain penetration length L_{B} can be actually stable under different values of magnetic field and, similarly, the same magnetic field can stabilize ChB with different values of L_{B} (see Supplementary Fig. 6). This is due to the pinning effect of BP in the thickness direction. The origin of the pinning effects in both lateral and thickness directions results from the crystal field in real materials, which is mimicked by the spatial discretization in our simulation[34]. In order to analyze the influences of the penetration length and the external magnetic field on the critical driving field of ChB motion, the results of ChB with different values of L_{B} and H_{ex} are plotted in Fig. 5a. The extracted critical driving fields are plotted as a function of penetration length and described nicely by a linear fitting in Fig. 5b, while the external field plays only a marginal role on the threshold. In general, the motion of a longer ChB requires a smaller driving field, as it contains more skyrmions to generate a stronger driving force. Such a relation may be useful to distinguish ChBs from SkTs and estimate the penetration length of ChBs in the experiment. Above the threshold of the driving field, the skyrmions of each layer in a ChB still display internal rotations relative to the BP shown in Fig. 2a. The missing ChB data in the strong driving regime in Fig. 5a is because the ChBs under such large driving

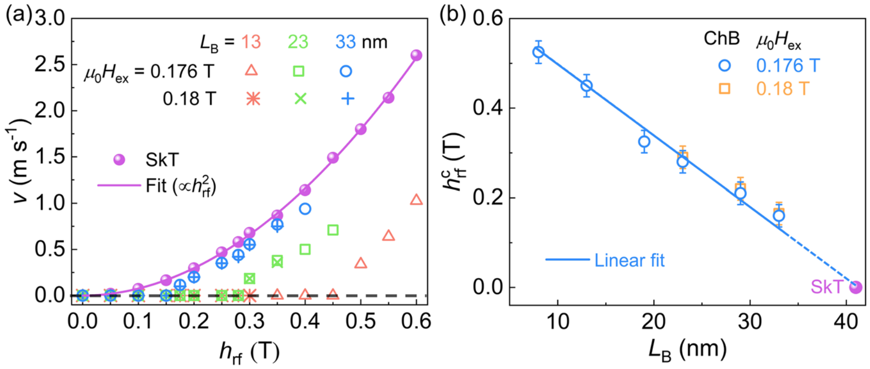

Fig. 5 | Velocities of chiral bobber (ChB)/skyrmion tube (SkT) and the threshold of the driving field for the ChB motion. a The velocities of the SkT and ChBs with different penetration lengths L_B as functions of the driving field h_{rf}. The solid curve corresponds to a fitting of the SkT velocity with a quadratic function. **b** Threshold of the driving field h_{rf}^c for the ChB motion as a function of penetration length. The blue solid line is a linear fit of the ChB data and the dashed line shows the extrapolation to the length of the SkT. The error bars in **b** represent half of the step size (0.025 T) of the magnetic field during the calculation.

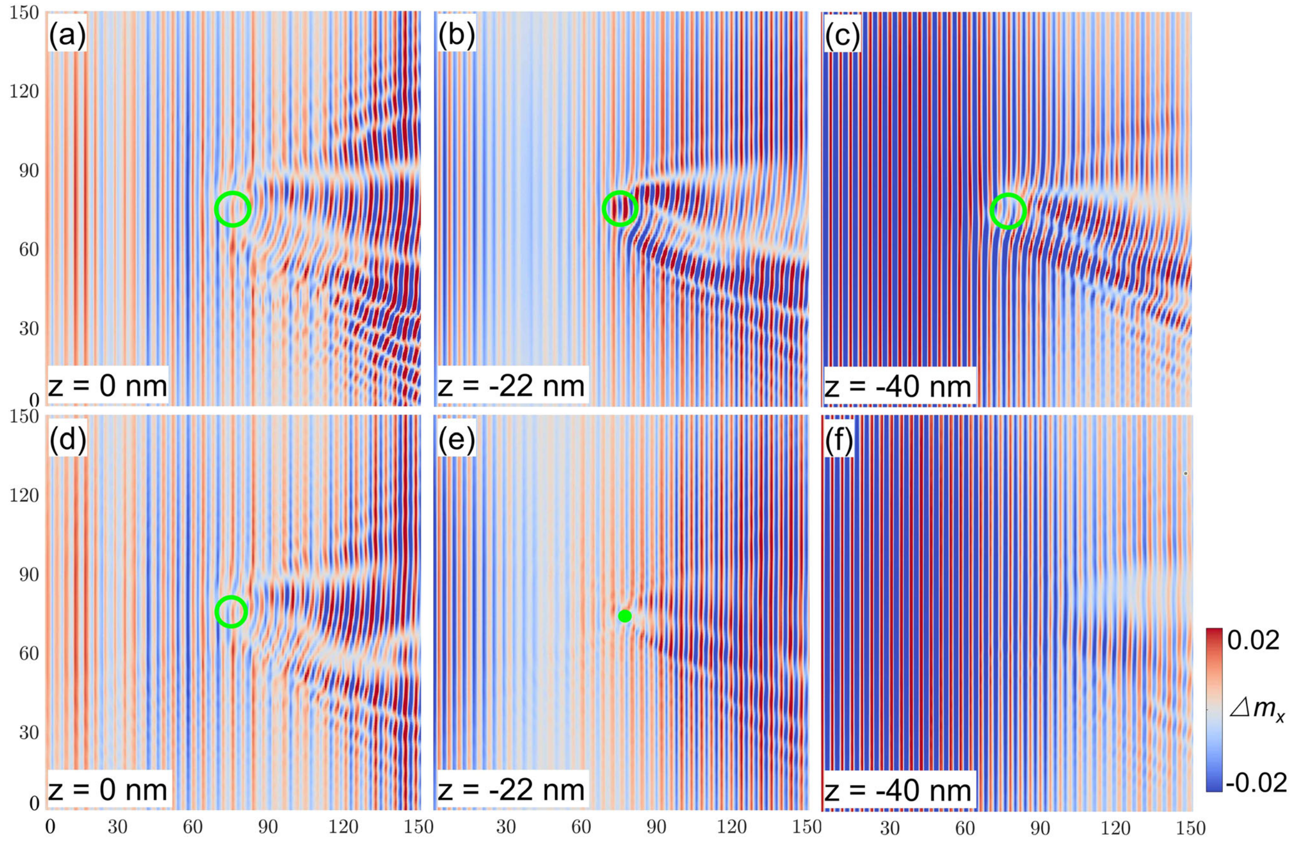

Fig. 6 | Scattering of spin waves by skyrmion tube and chiral bobber. Scattered spin-wave patterns of **a**–**c** skyrmion tube and **d**–**f** chiral bobber at different layers. The green circles in **a**–**d** and the solid green dot in **e** are defined as $m_z = 0$, indicating separately the location of skyrmions and the Bloch point in the corresponding layers. The color bar represents the x component of the dynamical magnetization.

fields become unstable. Note also that SkTs will also be destroyed by a too-strong driving field. The maximal velocity of SkTs is expected to be limited by the same mechanisms as those in the spin-wave-driven skyrmions in two dimensions ~100 m s^{-1}(ref. [61]). The quantitative evaluation of the maximal value requires a systematical simulation and is left for future study.

Scattering of spin waves by SkT and ChB

Figure 6 plots the snapshots of real space spin-wave patterns scattered by SkT (Fig. 6a–c) and ChB (Fig. 6d–f), with the green circles and dot indicating the locations of the skyrmion and the BP, respectively. A general feature of the scattering patterns is that, in contrast to the highly asymmetric scattering commonly seen in 2D case (see Supplementary Fig. 7), the interference patterns of the scattered beams in the present 3D case are clearly visible on both sides of skyrmions (see Fig. 6a–d). In the meantime, even for SkT, the scattering patterns present a strong layer dependence, which can be attributed to the layer-dependent spin-wave intensity in the thickness direction shown in Fig. 3b. In addition, the spin-wave scattering near the BP point for the ChB in Fig. 6e is found to exhibit asymmetric pattern as well, indicating its deviation from the Rutherford-like scattering predicted previously[50]. This reflects the influence of the neighboring skyrmions, which are closely connected with the BP.

Conclusions

In summary, we have demonstrated that ChB and SkT can be driven by spin waves in 3D systems. Bulk DMI causes nonuniform spin-wave intensity in the thickness direction, resulting in tornado-like dynamics of SkT and ChB. In contrast to the vanishing threshold of driving power for SkT motion, ChB can gain a finite velocity only when the driving power is beyond a critical value, which depends linearly on the penetration length of ChB. These reveal the potential directions to experimentally distinguish SkT and ChB. As a back action, the spin waves are scattered by SkT and ChB with the scattering spectrum distinguished from the 2D skyrmions and a symmetric Rutherford-like pattern from a single individual BP. The rich dynamics of ChB and SkT provide opportunities for exploring spin-wave devices and other spintronics applications.

Methods

Micromagnetic simulations

The stable magnetic textures are simulated by numerically solving the Landau-Lifshitz-Gilbert equation[71,72]:

$$\frac{d\mathbf{m}}{dt} = -\gamma\mathbf{m}\times\mathbf{B}_{\text{eff}} + \alpha\mathbf{m}\times\frac{d\mathbf{m}}{dt}, \tag{4}$$

where γ is the gyromagnetic ratio, α is the Gilbert damping constant and $\mathbf{B}_{\text{eff}} = -\delta\mathscr{H}/\left(M_s\delta\mathbf{m}\right)$ is the effective magnetic field. In our simulation, we take $A = 0.1$ pJ m^{-1}, $K_u = 5$ kJ m^{-3}, $M_s = 100$ kA m^{-1}, $D = 0.05$ mJ m^{-2} (ref. [26]), and an experimentally accessible damping coefficient $\alpha = 0.001$[73–75]. With these parameters, the discrimination parameter for isolated skyrmions is estimated to be $\pi^2D^2/(16AK_u) > 1$[76], suggesting the necessity of a proper external magnetic field to stabilize an isolated circular skyrmion, which is confirmed by our simulation. The magnetic film with the size of $300\times300\times41$ nm^3 is discretized by $1\times1\times1$ nm^3 units.

Data availability

The data supporting the findings of this study are available within this article and its Supplementary Information. Additional data that support the findings of this study are available from the corresponding author on reasonable requests.

Code availability

The micromagnetic simulation software MUMAX3 used in this work is open-source and can be accessed freely at http://mumax.github.io/.

Received: 13 November 2023; Accepted: 26 March 2024;
Published online: 04 April 2024

References

1. Rößler, U. K., Bogdanov, A. N. & Pfleiderer, C. Spontaneous skyrmion ground states in magnetic metals. *Nature* **442**, 797–801 (2006).
2. Fert, A., Reyren, N. & Cros, V. Magnetic skyrmions: advances in physics and potential applications. *Nat. Rev. Mater.* **2**, 1–15 (2017).
3. Reichhardt, C., Reichhardt, C. J. O. & Milovsević, M. V. Statics and dynamics of skyrmions interacting with disorder and nanostructures. *Rev. Mod. Phys.* **94**, 035005 (2022).
4. Park, J. P. & Crowell, P. A. Interactions of spin waves with a magnetic vortex. *Phys. Rev. Lett.* **95**, 167201 (2005).
5. Choe, S.-B. et al. Vortex core-driven magnetization dynamics. *Science* **304**, 420–422 (2004).
6. Van Waeyenberge, B. et al. Magnetic vortex core reversal by excitation with short bursts of an alternating field. *Nature* **444**, 461–464 (2006).
7. Shinjo, T., Okuno, T., Hassdorf, R., Shigeto, K. & Ono, T. Magnetic vortex core observation in circular dots of permalloy. *Science* **289**, 930–932 (2000).
8. Ohara, K. et al. Reversible transformation between isolated skyrmions and bimerons. *Nano Lett.* **22**, 8559–8566 (2022).
9. Göbel, B., Mook, A., Henk, J., Mertig, I. & Tretiakov, O. A. Magnetic bimerons as skyrmion analogues in in-plane magnets. *Phys. Rev. B* **99**, 060407 (2019).
10. Yu, X. Z. et al. Transformation between meron and skyrmion topological spin textures in a chiral magnet. *Nature* **564**, 95–98 (2018).
11. Wang, X. R., Hu, X. C. & Wu, H. T. Stripe skyrmions and skyrmion crystals. *Commun. Phys.* **4**, 1–7 (2021).
12. Wu, H., Hu, X., Jing, K. & Wang, X. R. Size and profile of skyrmions in skyrmion crystals. *Commun. Phys.* **4**, 1–7 (2021).
13. Hu, X.-C., Wu, H.-T. & Wang, X. R. A theory of skyrmion crystal formation. *Nanoscale* **14**, 7516–7529 (2022).
14. Wang, X. R. & Hu, X. C. Particle-continuum duality of skyrmions. *Phys. Rev. B* **107**, 174412 (2023).
15. Foster, D. et al. Two-dimensional skyrmion bags in liquid crystals and ferromagnets. *Nat. Phys.* **15**, 655–659 (2019).
16. Rybakov, F. N. & Kiselev, N. S. Chiral magnetic skyrmions with arbitrary topological charge. *Phys. Rev. B* **99**, 064437 (2019).
17. Hassan, M. et al. Dipolar skyrmions and antiskyrmions of arbitrary topological charge at room temperature. *Nat. Phys*. https://doi.org/10.1038/s41567-023-02358-z (2024).
18. Nagaosa, N. & Tokura, Y. Topological properties and dynamics of magnetic skyrmions. *Nat. Nanotechnol.* **8**, 899–911 (2013).
19. Fert, A., Cros, V. & Sampaio, J. Skyrmions on the track. *Nat. Nanotechnol.* **8**, 152–156 (2013).
20. Sampaio, J., Cros, V., Rohart, S., Thiaville, A. & Fert, A. Nucleation, stability and current-induced motion of isolated magnetic skyrmions in nanostructures. *Nat. Nanotechnol.* **8**, 839–844 (2013).
21. Yuan, H. Y., Wang, X. S., Yung, M.-H. & Wang, X. R. Wiggling skyrmion propagation under parametric pumping. *Phys. Rev. B* **99**, 014428 (2019).
22. Qiu, L. et al. Interlayer coupling effect on skyrmion dynamics in synthetic antiferromagnets. *Appl. Phys. Lett.* **118**, 082403 (2021).
23. Chen, J., Hu, J. & Yu, H. Chiral emission of exchange spin waves by magnetic skyrmions. *ACS Nano* **15**, 4372–4379 (2021).
24. Kent, N. et al. Creation and observation of hopfions in magnetic multilayer systems. *Nat. Commun.* **12**, 1562 (2021).
25. Zheng, F. et al. Hopfion rings in a cubic chiral magnet. *Nature* **623**, 718–723 (2023).
26. Saji, C., Troncoso, R. E., Carvalho-Santos, V. L., Altbir, D. & Nunez, A. S. Hopfion-driven magnonic hall effect and magnonic focusing. *Phys. Rev. Lett.* **131**, 166702 (2023).
27. Liu, Y., Watanabe, H. & Nagaosa, N. Emergent magnetomultipoles and nonlinear responses of a magnetic hopfion. *Phys. Rev. Lett.* **129**, 267201 (2022).
28. Tai, J.-S. B., Wu, J.-S. & Smalyukh, I. I. Geometric transformation and three-dimensional hopping of Hopf solitons. *Nat. Commun.* **13**, 2986 (2022).
29. Li, S. et al. Mutual conversion between a magnetic Néel hopfion and a Néel toron. *Phys. Rev. B* **105**, 174407 (2022).
30. Hu, Q. et al. Unidirectional current-driven toron motion in a cylindrical nanowire. *Appl. Phys. Lett.* **118**, 022404 (2021).
31. Zheng, F. et al. Experimental observation of chiral magnetic bobbers in B20-type FeGe. *Nat. Nanotechnol.* **13**, 451–455 (2018).
32. Ran, K. et al. Creation of a chiral bobber lattice in helimagnet-multilayer heterostructures. *Phys. Rev. Lett.* **126**, 017204 (2021).
33. Redies, M. et al. Distinct magnetotransport and orbital fingerprints of chiral bobbers. *Phys. Rev. B* **99**, 140407 (2019).
34. Gong, Z. et al. Current-induced dynamics and tunable spectra of a magnetic chiral bobber. *Phys. Rev. B* **104**, L100412 (2021).
35. Donnelly, C. et al. Time-resolved imaging of three-dimensional nanoscale magnetization dynamics. *Nat. Nanotechnol.* **15**, 356–360 (2020).
36. Shigenaga, T. & Leonov, A. O. Harnessing skyrmion Hall effect by thickness gradients in wedge-shaped samples of cubic helimagnets. *Nanomaterials* **13**, 2073 (2023).

37. Voinescu, R., Tai, J.-S. B. & Smalyukh, I. I. Hopf solitons in helical and conical backgrounds of chiral magnetic solids. *Phys. Rev. Lett.* **125**, 057201 (2020).
38. Jena, J. et al. Observation of fractional spin textures in a Heusler material. *Nat. Commun.* **13**, 2348 (2022).
39. Zheng, F. et al. Magnetic skyrmion braids. *Nat. Commun.* **12**, 5316 (2021).
40. Tai, J.-S. B. & Smalyukh, I. I. Static hopf solitons and knotted emergent fields in solid-state noncentrosymmetric magnetic nanostructures. *Phys. Rev. Lett.* **121**, 187201 (2018).
41. Li, Y. et al. Tunable terahertz oscillation arising from Bloch-point dynamics in chiral magnets. *Phys. Rev. Res.* **2**, 033006 (2020).
42. Raftrey, D. & Fischer, P. Field-driven dynamics of magnetic hopfions. *Phys. Rev. Lett.* **127**, 257201 (2021).
43. Im, M.-Y. et al. Dynamics of the Bloch point in an asymmetric permalloy disk. *Nat. Commun.* **10**, 1–8 (2019).
44. Xia, J., Zhang, X., Liu, X., Zhou, Y. & Ezawa, M. Nonlinear dynamics of the topological helicity wave in a frustrated skyrmion string. *Phys. Rev. B* **106**, 054414 (2022).
45. Seki, S. et al. Propagation dynamics of spin excitations along skyrmion strings. *Nat. Commun.* **11**, 256 (2020).
46. Wang, X. S., Qaiumzadeh, A. & Brataas, A. Current-driven dynamics of magnetic hopfions. *Phys. Rev. Lett.* **123**, 147203 (2019).
47. Rybakov, F. N., Borisov, A. B., Blügel, S. & Kiselev, N. S. New type of stable particle like states in chiral magnets. *Phys. Rev. Lett.* **115**, 117201 (2015).
48. Ahmed, A. S. et al. Chiral bobbers and skyrmions in epitaxial FeGe/Si(111) films. *Phys. Rev. Mater.* **2**, 041401 (2018).
49. Li, W. et al. Anatomy of skyrmionic textures in magnetic multilayers. *Adv. Mater.* **31**, 1807683 (2019).
50. Elías, R. G., Carvalho-Santos, V. L., Núñez, A. S. & Verga, A. D. Spin waves scattering on a Bloch point. *Phys. Rev. B* **90**, 224414 (2014).
51. Kim, S. K. & Tchernyshyov, O. Pinning of a Bloch point by an atomic lattice. *Phys. Rev. B* **88**, 174402 (2013).
52. Yu, X. Z. et al. Real-space observation of a two-dimensional skyrmion crystal. *Nature* **465**, 901–904 (2010).
53. Mühlbauer, S. et al. Skyrmion lattice in a chiral magnet. *Science* **323**, 915–919 (2009).
54. Charilaou, M. Prediction of confined and controllable Bloch points in nanocubes of chiral magnets. *Phys. Rev. B* **102**, 014430 (2020).
55. Liu, Y., Hou, W., Han, X. & Zang, J. Three-dimensional dynamics of a magnetic hopfion driven by spin transfer torque. *Phys. Rev. Lett.* **124**, 127204 (2020).
56. Zhu, J. et al. Current-driven transformations of a skyrmion tube and a bobber in stepped nanostructures of chiral magnets. *Sci. China Phys. Mech. Astron.* **64**, 227511 (2020).
57. Tang, J. et al. Magnetic skyrmion bundles and their current-driven dynamics. *Nat. Nanotechnol.* **16**, 1086–1091 (2021).
58. Xia, J. et al. Current-induced dynamics of skyrmion tubes in synthetic antiferromagnetic multilayers. *Phys. Rev. B* **103**, 174408 (2021).
59. Iwasaki, J., Beekman, A. J. & Nagaosa, N. Theory of magnon-skyrmion scattering in chiral magnets. *Phys. Rev. B* **89**, 064412 (2014).
60. Psaroudaki, C. & Loss, D. Skyrmions driven by intrinsic magnons. *Phys. Rev. Lett.* **120**, 237203 (2018).
61. Zhang, X. et al. Motion of skyrmions in nanowires driven by magnonic momentum-transfer forces. *N. J. Phys.* **19**, 065001 (2017).
62. Yan, P., Wang, X. S. & Wang, X. R. All-magnonic spin-transfer torque and domain wall propagation. *Phys. Rev. Lett.* **107**, 177207 (2011).
63. Komineas, S. & Papanicolaou, N. Skyrmion dynamics in chiral ferromagnets. *Phys. Rev. B* **92**, 064412 (2015).
64. Wang, C., Xiao, D., Chen, X., Zhou, Y. & Liu, Y. Manipulating and trapping skyrmions by magnetic field gradients. *N. J. Phys.* **19**, 083008 (2017).
65. Weißenhofer, M. & Nowak, U. Temperature dependence of current-driven and Brownian skyrmion dynamics in ferrimagnets with compensation point. *Phys. Rev. B* **107**, 064423 (2023).
66. Zhang, X., Zhou, Y. & Ezawa, M. Magnetic bilayer-skyrmions without skyrmion Hall effect. *Nat. Commun.* **7**, 10293 (2016).
67. Shen, L. & Shen, K. Skyrmion-based chaotic oscillator driven by a constant current. *Phys. Rev. B* **109**, 014422 (2024).
68. Dohi, T., DuttaGupta, S., Fukami, S. & Ohno, H. Formation and current-induced motion of synthetic antiferromagnetic skyrmion bubbles. *Nat. Commun.* **10**, 5153 (2019).
69. Jiang, W. et al. Skyrmions in magnetic multilayers. *Phys. Rep.* **704**, 1–49 (2017).
70. Legrand, W. et al. Room-temperature stabilization of antiferromagnetic skyrmions in synthetic antiferromagnets. *Nat. Mater.* **19**, 34–42 (2020).
71. Gilbert, T. A phenomenological theory of damping in ferromagnetic materials. *IEEE Trans. Magn.* **40**, 3443–3449 (2004).
72. Vansteenkiste, A. et al. The design and verification of MuMax3. *AIP Adv.* **4**, 107133 (2014).
73. Wang, H. et al. Chiral spin-wave velocities induced by all-garnet interfacial Dzyaloshinskii-Moriya interaction in ultrathin yttrium iron garnet films. *Phys. Rev. Lett.* **124**, 027203 (2020).
74. Schoen, M. A. W. et al. Ultra-low magnetic damping of a metallic ferromagnet. *Nat. Phys.* **12**, 839–842 (2016).
75. Zhang, Y. et al. Strain-driven Dzyaloshinskii-Moriya interaction for room-temperature magnetic skyrmions. *Phys. Rev. Lett.* **127**, 117204 (2021).
76. Wang, X. S., Yuan, H. Y. & Wang, X. R. A theory on skyrmion size. *Commun. Phys.* **1**, 31 (2018).

Acknowledgements

This work is supported by the National Natural Science Foundation of China (Grants No.11974047 and No.12374100) and the Fundamental Research Funds for the Central Universities.

Author contributions

K.S. coordinated the project. L.Q. and L.S. performed the numerical simulations and theoretical calculations. L.Q. and K.S. wrote the manuscript with useful comments from L.S.

Competing interests

The authors declare no competing interests.

Additional information

Supplementary information The online version contains supplementary material available at https://doi.org/10.1038/s42005-024-01608-7.

Correspondence and requests for materials should be addressed to Ka Shen.

Peer review information *Communications Physics* thanks Yan Zhou and the other, anonymous, reviewer(s) for their contribution to the peer review of this work.

Reprints and permissions information is available at http://www.nature.com/reprints

Publisher's note Springer Nature remains neutral with regard to jurisdictional claims in published maps and institutional affiliations.

Open Access This article is licensed under a Creative Commons Attribution 4.0 International License, which permits use, sharing, adaptation, distribution and reproduction in any medium or format, as long as you give appropriate credit to the original author(s) and the source, provide a link to the Creative Commons licence, and indicate if changes were made. The images or other third party material in this article are included in the article's Creative Commons licence, unless indicated otherwise in a credit line to the material. If material is not included in the article's Creative Commons licence and your intended use is not permitted by statutory regulation or exceeds the permitted use, you will need to obtain permission directly from the copyright holder. To view a copy of this licence, visit http://creativecommons.org/licenses/by/4.0/.

© The Author(s) 2024